# Three-dimensional computational modeling of multiple deformable cells flowing in microvessels

Sai K. Doddi and Prosenjit Bagchi*
*Department of Mechanical and Aerospace Engineering, Rutgers University–The State University of New Jersey, Piscataway, New Jersey 08854, USA*

(Received 13 October 2008; revised manuscript received 3 February 2009; published 21 April 2009)

Three-dimensional (3D) computational modeling and simulation are presented on the motion of a large number of deformable cells in microchannels. The methodology is based on an immersed boundary method, and the cells are modeled as liquid-filled elastic capsules. The model retains two important features of the blood flow in the microcirculation, that is, the particulate nature of blood and deformation of the erythrocytes. The tank-treading and tumbling motion and the lateral migration, as observed for erythrocytes in dilute suspension, are briefly discussed. We then present results on the motion of multiple cells in semidense suspension and study how their collective dynamics leads to various physiologically relevant processes such as the development of the cell-free layer and the Fahraeus-Lindqvist effect. We analyze the 3D trajectory and velocity fluctuations of individual cell in the suspension and the plug-flow velocity profile as functions of the cell deformability, hematocrit, and vessel size. The numerical results allow us to directly obtain various microrheological data, such as the width of the cell-free layer, and the variation in the apparent blood viscosity and hematocrit over the vessel cross section. We then use these results to calculate the core and plasma-layer viscosity and show that the two-phase (or core-annular) model of blood flow in microvessels underpredicts the blood velocity obtained in the simulations by as much as 40%. Based on *a posteriori* analysis of the simulation data, we develop a three-layer model of blood flow by taking into consideration the smooth variation in viscosity and hematocrit across the interface of the cell-free layer and the core. We then show that the blood velocity predicted by the three-layer model agrees very well with that obtained from the simulations.

DOI: 10.1103/PhysRevE.79.046318 PACS number(s): 47.63.−b, 47.61.Jd

## I. INTRODUCTION

Computational modeling and simulation of blood flow in microcirculation are major challenges [1]. One reason is that blood in small vessels behaves as a multiphase suspension of deformable particles. The particulate phase of blood is primarily made of erythrocytes, leukocytes, and platelets. Erythrocytes are the major constituent of blood accounting for 40–45% of the total volume. Normal healthy erythrocytes are extremely deformable when subject to shear. Rheology of blood in microcirculation is primarily determined by the deformability of the erythrocytes and the multiphase nature of blood.

Experiments on blood flow in microvessels having internal diameter of 10–300 $\mu$m have revealed complex rheological behavior [2–4], such as the Fahraeus-Lindqvist effect [5] which refers to a decrease in the apparent viscosity of blood with decreasing vessel diameter. The physical mechanism giving rise to the Fahraeus-Lindqvist effect is believed to be an axial streaming (or a lateral migration) of the erythrocytes causing a cell-depleted region near the wall [6–10]. Among others, the factors that cause the axial streaming are the extreme deformability of the erythrocytes [11] and the reduced gradient of shear away from the vessel wall. It has been observed for erythrocytes in dilute suspension by many researchers including Goldsmith [12]. In whole blood, which is a semidense suspension, a continuous lateral migration of the erythrocytes is not observed. Rather, the cells are intermittently dispersed by the hydrodynamic interaction from the neighboring cells. The cell-free layer then develops under a balance of the lateral migration and the hydrodynamic dispersion.

A continuum model of blood flow in microvessels, such as the core-annular (or two-phase) model [13–15], is sufficient to qualitatively predict the Fahraeus-Lindqvist effect. Such models, however, rely on estimates of various physiological parameters, such as the width of the cell-free layer, which can be obtained only by high-resolution experiments [4,7,10], or computational simulations in which the motion and deformation of individual cell are fully resolved. Theoretical and computational modeling and simulation have so far considered dilutely suspended cells in shear flows [16–21] and axisymmetric and nonaxisymmetric single-file motions of cells in narrow tubes and channels [8,15,22–27]. Extension of such models to a large number of cells, without sacrificing the detailed mechanics, has remained a major computational challenge.

Recent advances in numerical methods and computational resources have enabled researchers to consider such large-scale simulations. Sun and Munn [28] used a lattice-Boltzmann simulation to address blood flow in 20–40 $\mu$m wide channels by modeling the cells as two-dimensional (2D) rigid disks. Zhang *et al.* [29] developed a 2D immersed boundary lattice-Boltzmann technique that can simulate flow of a small number of deformable erythrocytes. Bagchi [30] used an immersed boundary method in 2D to simulate the motion of a large number (up to 2500) of deformable erythrocytes in 10–300 $\mu$m vessels. Ding and Aidun [31] used a three-dimensional (3D) lattice-Boltzmann technique to consider cluster formation in a large ensemble of deformable erythrocytes in pressure-driven flow. Dupin *et al.* [32] presented the 3D lattice-Boltzmann simulations of up to 200

*Corresponding author; pbagchi@jove.rutgers.edu

 

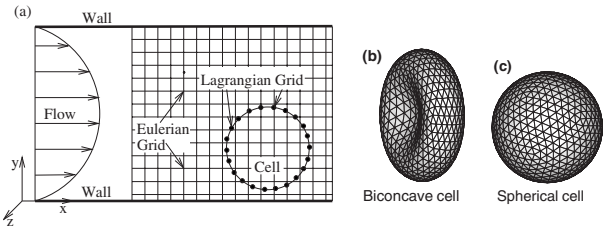


FIG. 1. The schematic of the microchannel with parabolic flow and the Eulerian (fixed) and Lagrangian (moving) meshes. The 3D surface discretization for the spherical and biconcave cells is also shown.

deformable erythrocytes in suspension. Pivkin *et al.* [33] developed a dissipative-particle-dynamics technique to consider the simultaneous motion of deformable erythrocytes and their effect on platelet deposition and thrombus formation. Freund [34] studied the margination of the leukocytes in presence of deformable erythrocytes in a 2D microvessel using a boundary-integral technique. Zhao *et al.* [35] developed a fixed-mesh method for the study of deformable fluid-structure interaction in 3D with application to biological systems.

In this paper, we present 3D computational modeling and simulation of a large number of deformable cells, up to 122 in number, flowing in microchannels. We analyze the trajectory and velocity fluctuations of individual cells in the suspension and the plug-flow velocity profile as functions of the cell deformability, hematocrit, and channel width. Comparison with *in vitro* [3] and *in vivo* [10,36,37] data is presented. The simulations allow us to directly obtain the width of the cell-free layer which is a physiologically important parameter. We then use these results to show that the two-phase (or core-annular) model for blood flow in microvessels underpredicts the blood velocity obtained in the simulations. Based on *a posteriori* analysis of the simulation data, we develop a three-layer model for blood flow in microvessel. We then show that the blood velocity predicted by the three-layer model agrees very well with that obtained from the simulations.

## II. SIMULATION TECHNIQUE

### A. Problem setup

The flow configuration (Fig. 1) and the simulation technique are the 3D version of our previous 2D study [30]. We consider the motion of a large number of deformable cells suspended in a microchannel bounded by two parallel plates. Thus the motion of the cells considered here is more representative of the Fung-Sobin model [38] of the pulmonary circulation than that of the normal systematic microcirculation. The distance between the plates is $H$. The plates are parallel to the $x$ and $z$ axes as shown in Fig. 1(a). The flow is driven by a constant *mean* pressure gradient $-d\bar{P}/dx$. In absence of the cells, the undisturbed flow $\mathbf{u}_p$ is a fully developed parabolic (Poiseuille) flow of pure plasma and is directed from $x=-\infty$ to $x=+\infty$ as

$$\mathbf{u}_p = \left[ \frac{1}{2\mu_p}\left(-\frac{d\bar{P}}{dx}\right)(Hy - y^2), 0, 0 \right], \tag{1}$$

where $\mu_p = 1.2$ cP is the plasma viscosity. The computation domain is a cube of sides of length $H$ which is bounded by the plates in the $y$ direction and is *open* in $x$ and $z$ directions. At the top and bottom plates, no-slip conditions are imposed. Periodic conditions are imposed at the inflow (left) and outflow (right) boundaries of the domain. The cells that leave the domain through the outflow boundary are introduced back into the domain through the inflow boundary. Periodic conditions are also imposed at the boundaries in the $z$ direction.

### B. Rheological models for cells

On a mesoscopic scale, the detailed molecular structure of a cell membrane can be neglected, and the entire cell can be modeled as a *capsule*, that is, a liquid drop made of hemoglobin and surrounded by an infinitesimally thin elastic membrane. We consider two different undeformed shapes of cells: spherical and biconcave. For the spherical cells, the viscosities of the interior and exterior fluids are assumed to be the same and equal to the plasma viscosity of 1.2 cP. For the biconcave cells, the viscosities of the interior and exterior fluids are taken to be 6 and 1.2 cP, respectively, as in case of normal erythrocytes and plasma. The elastic force generated in the membrane during cell deformation can be obtained by knowing the strain energy function $W$ of the membrane material. Several forms of $W$ have been proposed for erythrocyte membranes [39,40]. Here we consider the neo-Hookean law,

$$W = \frac{E_s}{6}(\epsilon_1^2 + \epsilon_2^2 + \epsilon_1^{-2}\epsilon_2^{-2} - 3), \tag{2}$$

where $E_s$ is the shear modulus and $\epsilon_1$ and $\epsilon_2$ are the principal strains. The resistance to dilatation is imposed for the biconcave cells by adding a term $E_D(\epsilon_1\epsilon_2 - 1)^2$ [40] to Eq. (2) where $E_D$ is the membrane area dilatation modulus. The membrane of an erythrocyte also exhibits bending resistance and viscoelasticity which are neglected in our model. The bending energy can be approximated as $k_b(\kappa - \kappa_0)^2$, where $\kappa$ and $\kappa_0$ are the membrane curvatures in the deformed and spontaneous conditions, and the bending rigidity $k_b \sim 0.2 \times 10^{-19}$ J [41]. In order for the bending energy to be of the same order as the elastic energy, $\kappa/\kappa_0$ has to be $3 \times 10^3$ if we take a reasonable estimate of $\kappa_0 \sim 1$ $\mu$m. *A posteriori* calculation of biconcave cells in suspension (Fig. 8) suggests that $\kappa/\kappa_0$ is significantly smaller than the above value, implying that the effect of bending resistance is small when cell motion in gaps much larger than the characteristic cell size is considered at low shear as is the case in our problem. The strain energy function given above does not by itself differentiate between various unstressed shapes (e.g., spherical versus biconcave). It only models the elastic energy developed as the particle deforms from its given shape at $t=0$ [at resting, $W(t=0)=0$]. Our approach is different from that taken by many previous authors where the energy minimization is used to drive an initially spherical particle into a bi-

concave shape [42]. Instead, we specify an analytical form of the biconcave shape at $t=0$ as

$$x = R_0 x', \quad y = \tfrac{1}{2} R_0 (1 - r^2)^{1/2} (C_0 + C_2 r^2 + C_4 r^4), \quad z = R_0 z', \tag{3}$$

where $x,y,z$ are the coordinates of the cell surface, $x',y',z'$ are the surface coordinates of a unit sphere, $R_0$ is a constant to preserve the volume, $r^2 = x'^2 + z'^2$, $C_0 = 0.32$, $C_2 = 2.003$, and $C_4 = -1.123$ [26,43].

### C. Front-tracking method

The coupling between the cell deformation and the fluid flow is done using a front-tracking technique developed by Tryggvason *et al.* [44] that is based on the immersed boundary method pioneered by Peskin and Miller [45,46]. In this method, the flow field is discretized using a fixed (Eulerian) mesh, and the cell surface is discretized using a moving (Lagrangian) mesh (Fig. 1). Then the motion of the exterior fluid (plasma) and interior fluid (hemoglobin) can be expressed using a single set of equations. The fluid/structure coupling is done by a body force $\mathbf{F}(\mathbf{x},t)$ which is related to the elastic force $\mathbf{f}(\mathbf{x}',t)$ generated in the cell membrane as

$$\mathbf{F}(\mathbf{x},t) = \int_{\partial S} \mathbf{f}(\mathbf{x}',t)\, \delta(\mathbf{x} - \mathbf{x}')\, d\mathbf{x}', \tag{4}$$

where $\mathbf{x}$ is the Eulerian grid, $\mathbf{x}'$ is a Lagrangian point on the cell surface, $\partial S$ is the entire cell surface, and $\delta$ is the 3D delta function.

We assume that both the plasma and hemoglobin solutions are incompressible and Newtonian fluids. The Newtonian nature of these fluids is well established [43]. The non-Newtonian nature of the whole blood arises due to its particulate nature. The fluid motion is governed by the continuity and Navier-Stokes equations as

$$\nabla \cdot \mathbf{u} = 0, \quad \rho \left[ \frac{\partial \mathbf{u}}{\partial t} + \mathbf{u} \cdot \nabla \mathbf{u} \right] = -\nabla p - \frac{d\bar{P}}{dx} \mathbf{e}_x + \nabla \cdot \tau + \mathbf{F}, \tag{5}$$

where $\mathbf{u}(\mathbf{x},t)$ is the fluid velocity, $\rho$ is the density, $p$ is a local pressure, $\mathbf{e}_x$ is the unit vector along the $x$ axis, and

$$\tau = \mu [\nabla \mathbf{u} + (\nabla \mathbf{u})^T] \tag{6}$$

is the viscous stress tensor. $\mu(\mathbf{x},t)$ is the viscosity in the entire fluid which can be written as

$$\mu(\mathbf{x},t) = \mu_p [1 + (\lambda - 1) I(\mathbf{x},t)], \tag{7}$$

where $\lambda \mu_p$ is the viscosity of the cytoplasmic fluid and $I(\mathbf{x},t)$ is an indicator function which is 1 in the interior of a cell and 0 outside. For the spherical cells, we take $\lambda = 1$ and for the biconcave cells $\lambda = 5$, as in the case of normal erythrocytes. Note that the net pressure gradient in Eq. (5) is the sum of the externally applied constant pressure gradient $-d\bar{P}/dx$ and the fluctuating local pressure gradient $-\nabla p$; the latter is generated due to the presence of the interacting cells. Using the Poiseuille law, $-d\bar{P}/dx = 8\mu_p U_{\mathrm{cl}}/H^2$, which is used in Eq. (5) as a known term. Periodic conditions are imposed explicitly on the fluid velocity and perturbation pressure $p$ by appropriately writing the derivative matrices in the advection/diffusion and pressure Poisson equations at the inlet/outlet boundaries.

The velocity of the cell surface is computed at each time step, after solving the Navier-Stokes equations, as

$$\mathbf{u}(\mathbf{x}',t) = \int_S \mathbf{u}(\mathbf{x},t)\, \delta(\mathbf{x} - \mathbf{x}')\, d\mathbf{x}, \tag{8}$$

where $S$ indicates the entire flow domain. The Lagrangian points on the membrane are then advected as

$$\frac{d\mathbf{x}'}{dt} = \mathbf{u}(\mathbf{x}',t). \tag{9}$$

As the cells move and deform, $\mu(\mathbf{x},t)$ is updated by solving a Poisson equation for the indicator function $I(\mathbf{x},t)$ as

$$\nabla^2 I = \nabla \cdot \mathbf{G}, \tag{10}$$

where $\mathbf{G} = \int_{\partial S} \delta(\mathbf{x} - \mathbf{x}') \mathbf{n}\, d\mathbf{x}'$ and $\mathbf{n}$ is the unit normal to the cell surface. For numerical implementation, a smooth representation of the $\delta$ function is used that spans over four Eulerian grids [44].

### D. Numerical treatment of membrane deformation

The force $\mathbf{f}(\mathbf{x}',t)$ generated in the cell membrane during deformation is obtained using a finite element model developed by Charrier *et al.* [47] and Shrivastava and Tang [48]. First, the cell surface is discretized using flat triangular elements (Fig. 1). The forces acting on the three vertices of a triangular element are obtained by computing the displacements of the vertices of the deformed element with respect to the undeformed element. For this purpose, the undeformed and deformed elements are transformed to a common plane using rigid-body rotations. The problem then reduces to a 2D (planar) deformation. Using the principle of virtual work, the in-plane force $\mathbf{f}^P$ at each vertex is obtained as

$$\mathbf{f}^P = \frac{\partial W}{\partial \epsilon_1} \frac{\partial \epsilon_1}{\partial \mathbf{v}} + \frac{\partial W}{\partial \epsilon_2} \frac{\partial \epsilon_2}{\partial \mathbf{v}}, \tag{11}$$

where $\mathbf{v}$ is the displacement of the vertex. Assuming that $\mathbf{v}$ varies linearly *inside* an element, a displacement gradient tensor $\mathbf{D}$ is obtained. The in-plane strains are related to $\mathbf{D}$ as

$$\epsilon_i^2 = \tfrac{1}{2} [G_{11} + G_{22} \pm \sqrt{\{(G_{11} - G_{22})^2 + 4G_{12}^2\}}], \quad i = 1,2, \tag{12}$$

where $\mathbf{G} = \mathbf{D}^{\mathrm{T}} \mathbf{D}$. The derivatives, such as $\partial \epsilon_1 / \partial \mathbf{v}$ in Eq. (11), can then be written explicitly, and hence $\mathbf{f}^P$ is determined. The in-plane force is then transformed to the global coordinates. The resultant force $\mathbf{f}(\mathbf{x}',t)$ at a Lagrangian node is obtained by the vector resultant of the forces contributed by all the elements which share that node.

### E. Dimensionless parameters

The centerline velocity of the parabolic flow of pure plasma is $U_{\mathrm{cl}}$. For the spherical cells, $d$ denotes the unde-

formed diameter. For the biconcave cells, $d$ is the largest end-to-end distance. The governing equations are made dimensionless using the channel width $H$ as the characteristic length scale, $U_{\rm cl}$ as the velocity scale, and $H/U_{\rm cl}$ as the time scale. The dimensionless time is denoted by $t^*$. The major dimensionless parameters are (i) the capillary number Ca $=\mu_p U_{\rm cl}/E_s$ which is the ratio of the viscous force in the fluid to the elastic force in the cell membrane, (ii) the ratio of the channel width to cell diameter $H/d$, and (iii) the volume fraction of the cells or the vessel hematocrit $H_t$. For a normal erythrocyte, $E_s \approx 6\times 10^{-3}$ dyn/cm [43]. Using $U_{\rm cl}=3$ mm/s and $\mu_p=1.2$ cP, we get Ca=0.6 for a normal cell. In our simulations Ca is varied from 0.005 to 0.6 in order to study the effect of cell deformability. Increasing Ca implies more deformable cells. For the spherical cells, the area dilatation modulus $E_D$ is neglected. For the biconcave cells, we take $E_D/E_s=100$. The size ratio $H/d$ is varied from 1.25 to 6.3 representing channel width in the range of 10–45 $\mu$m. The maximum vessel hematocrit $H_t$ is taken to be 26%, which gives a discharge hematocrit $H_d$ in the range of 28–34%. Though the convective terms in the Navier-Stokes equations are retained during the computations, the Reynolds number of the cell, defined as $\mathrm{Re}=\rho U_{\rm cl} d/\mu_p$, is around $10^{-2}$, and hence the effect of inertia is small.

### F. Flow solver and numerical resolution

The Navier-Stokes equations are discretized using a second-order finite difference scheme. For time marching, a second-order two-step time-split scheme is used. In the first step, an advection-diffusion equation is solved to predict a velocity field that is not incompressible. In the second step, the local pressure $p$ is obtained by solving a Poisson equation. Using the pressure, the velocity field is then corrected to make it divergence-free. For the spherical cells, the number of cells in the computational box varies from 1 to 122, as $H/d$ and $H_t$ are increased. For the biconcave cells, the number varies from 3 to 113. Table I lists the parameters and the resolution for all cases. For each case, at least three different Cas are simulated. The Eulerian resolution varies from $120\times 121\times 120$ to $240\times 241\times 240$. The Lagrangian resolution used is 1280–5120 triangular elements. Dimensionless time step is $10^{-3}$. The computation time is 24 h for a simulation of 122 cells up to $t^*\approx 15$ using eight 1.9 GHz IBM power 5 processors.

## III. VALIDATION

We validate by studying the deformation of an initially spherical capsule suspended in a linear shear flow. Details are in [49]. The capillary number is defined as Ca $=\dot{\gamma} d\mu_p/2E_s$, where $\dot{\gamma}$ is the shear rate. Figure 2(a) shows the time history of the Taylor deformation parameter $D=(L-B)/(L+B)$, where $L$ and $B$ are the major and minor axes of the deformed ellipsoid shape in the plane of shear. Excellent agreement is found between the present results and those of Ramanujan and Pozrikidis [17] who used a boundary-integral technique. Comparison with an experimental result [50] and an analytical result (for small deformation) [51] as given in Fig. 2(b) also suggests reasonable agreement. The change in the cell volume is less than $\pm 0.1\%$ from its initial volume. The projection method used here for the flow solver satisfies the mass conservation up to $\approx 10^{-14}$ at every grid point in the computational domain.

TABLE I. Size ratio ($H/d$), vessel hematocrit ($H_t$), number of cells per computational box ($N_c$), and Eulerian resolution used in the present simulations.

| | $H/d$ | $H_t$ (%) | $N_c$ | Resolution |
|---|---|---|---|---|
| Spherical cells | 6.3 | 26 | 122 | $160\times 161\times 160$ |
| | | 18 | 84 | |
| | | 12 | 56 | |
| | | 5 | 23 | |
| | 4.5 | 26 | 44 | $120\times 121\times 120$ |
| | | 18 | 30 | |
| | | 12 | 20 | |
| | | 5 | 8 | |
| | 4.5 | 18 | 30 | $240\times 241\times 240$ |
| | 4.5 | 18 | 120 | $240\times 121\times 240$ |
| | 3.1 | 26 | 15 | $120\times 121\times 120$ |
| | 2.4 | | 7 | |
| | 1.6 | | 2 | |
| | 1.25 | | 1 | |
| Biconcave cells | 4.9 | 26 | 113 | $160\times 161\times 160$ |
| | 3.1 | 26 | 31 | $120\times 121\times 120$ |
| | 2.5 | | 16 | |
| | 1.4 | | 3 | |

## IV. RESULTS AND DISCUSSION

### A. Isolated cell

First we consider the motion of a single isolated cell in the parabolic flow in the channel to show that our simulation can predict the lateral drift. Results for the spherical cell are

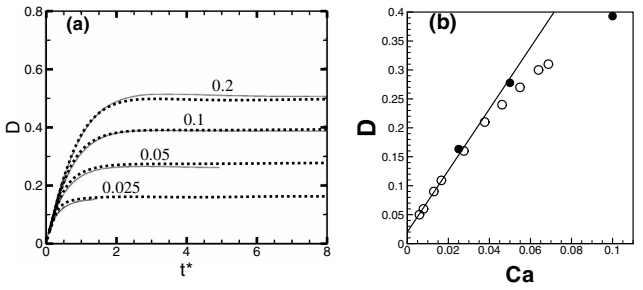


FIG. 2. Validation: deformation of an initially spherical cell in a linear shear flow. (a) History of deformation parameter $D$ for various Ca. The solid lines are the results from the boundary-integral simulations [17]; dotted lines are the present results. (b) Comparison of the present results (●) with experiments [50] (○) using polyamide microcapsules, and the analytical result [51] in the limit of small deformation which predicts $D=(25/4)$ Ca (—).

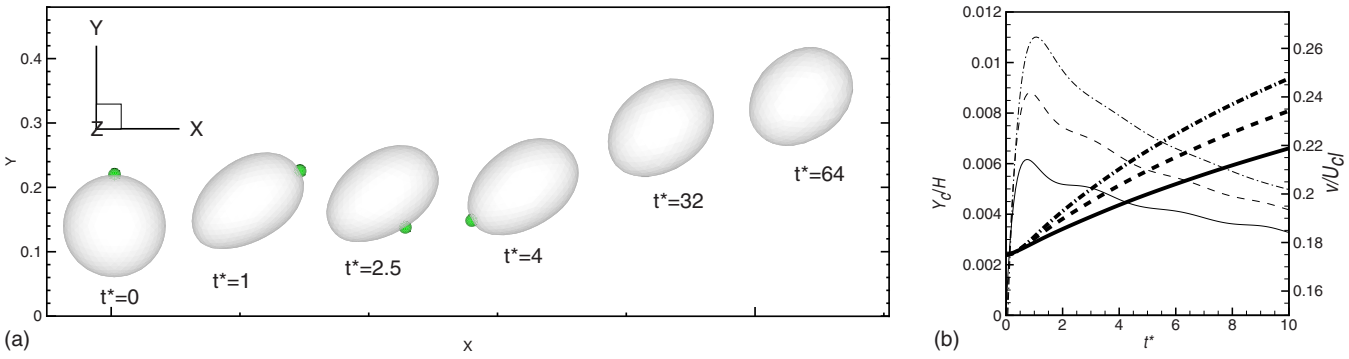


FIG. 3. (Color online) Lateral drift of a spherical cell in microchannel. The flow is from left to right. The cell is released at $y_c/H=0.175$ at $t^*=0$. (a) Cell shape and location for Ca=0.2 are shown at different times. Also shown is the membrane tank treading by a marker point. $y=0$ is the bottom wall and $y=0.5$ is the center of the channel. (b) Lateral location ($y_c/H$, thick lines) of the cell center of mass and lateral velocity ($v/U_{\mathrm{cl}}$, thin lines) with time for Ca=0.1 (——), Ca=0.2 (- - - - - -), and Ca=0.4 (-·-·-).

shown in Fig. 3 for $H/d=6.3$ and Ca=0.2. The cell is released close to the bottom wall at $t^*=0$, and the simulation continues until $t^*\approx 65$ when it reaches close to the center [Fig. 3(a)]. The cell membrane rotates in a tank-treading manner in the clockwise direction which is shown in Fig. 3(a) by following a marker point on the membrane. Figure 3(b) shows the history of the lateral position $y_c$ of the cell center of mass and the drift velocity $v$ for various Ca. The drift velocity increases with increasing Ca as the cell becomes more deformable.

The motion of a biconcave cell in the microchannel is shown in Fig. 4(a) for $H/d=3.1$ and Ca=0.1. The biconcave cell undergoes tumbling motion while moving axially with the flow. In experiments using erythrocytes, as well as

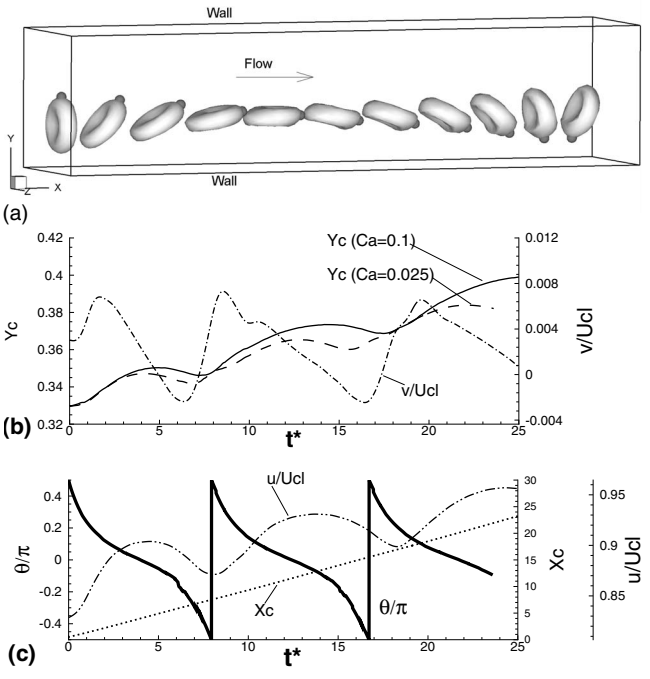


FIG. 4. (a) Tumbling motion of a biconcave cell in parabolic flow in the microchannel. A marker point on the cell surface is also indicated. (b) and (c) show cell trajectory ($x_c$ and $y_c$), velocity ($u/U_{\mathrm{cl}}$ and $v/U_{\mathrm{cl}}$), and angular orientation ($\theta/\pi$) with the $x$ axis.

spherical and nonspherical capsules and vesicles in dilute suspension, two modes of motion, tank-treading and tumbling, have been observed by previous researchers (see, e.g., [52]). The transition from the tank-treading mode to the tumbling mode occurs as λ and the aspect ratio increase. In the present simulations, $\lambda=1$ for the spherical cells and 5 for the biconcave cells. The results presented here are, therefore, in agreement with these previous observations. The time history of the axial ($x_c$) and lateral ($y_c$) positions of the center of mass and the axial and lateral velocity components ($u/U_{\mathrm{cl}}$ and $v/U_{\mathrm{cl}}$) is shown in Figs. 4(b) and 4(c). Also shown in Fig. 4(c) is the time-dependent angular orientation ($\theta/\pi$) that the major axis of the cell makes with the flow direction. The period of tumbling, when the cell is located close to the wall, is about $\dot{\gamma}T=32$ which compares well to 31.6 based on Jeffery's theory [53]. The drift velocity oscillates due to the tumbling motion. It is maximum when the major axis is aligned with the extensional direction of the flow and minimum when aligned with the compressional direction. Oscillations in the lateral velocity cause undulations in the lateral position. However, on the average, the cell drifts away from the wall. The oscillatory drifting motion predicted by the simulations agrees qualitatively with the glass tube experiments by Goldsmith [12] using dilute erythrocyte suspension.

The above results summarize the general characteristics of the motion of the deformable cells in a dilute suspension in a wall-bounded parabolic flow. We conclude that the present computational model is able to capture the general dynamical behavior, such as the tank-treading and the tumbling motion and the lateral drift of an erythrocyte in a shear flow.

### B. Partly dense suspension

Next we consider the single-file motion of cells which is observed during blood flow in narrow capillaries having diameter comparable or smaller than the erythrocyte diameter. In such vessels, cells squeeze to parachute shapes [9,22,23,26,54]. Results from our simulations are shown in Fig. 5(a) for an initially spherical cell of $H/d=1.25$ and for a vessel hematocrit $H_t=26\%$. The front and rear ends of the

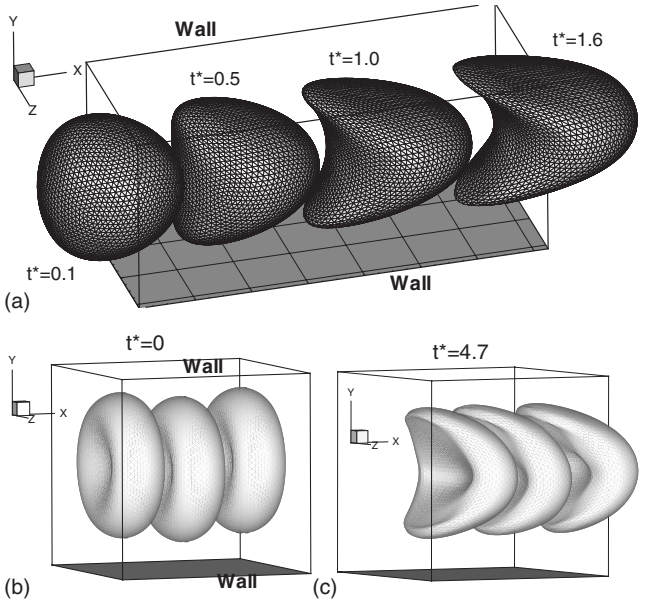


FIG. 5. Single-file motion: (a) transient deformation of a spherical cell of $H/d=1.25$ and Ca=0.6 in the channel. [(b) and (c)] deformation of biconcave cells for $H/d=1.4$ and Ca=0.6.

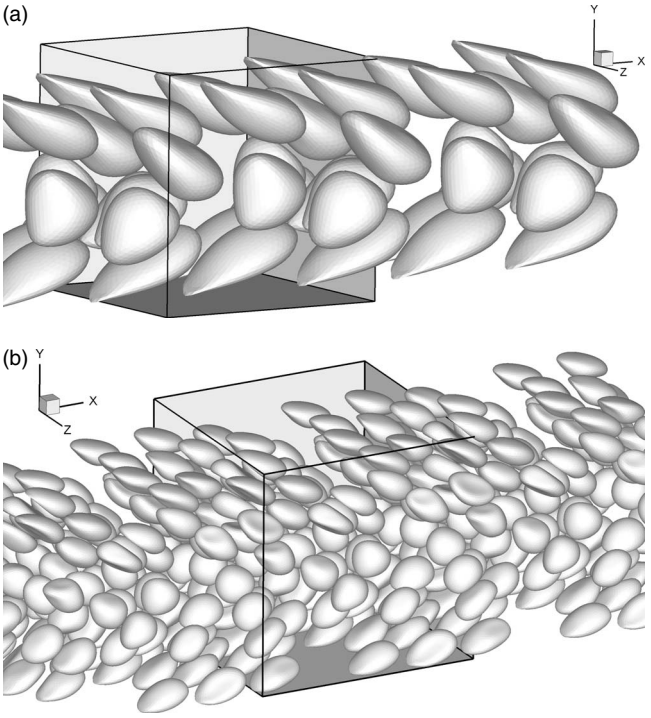


FIG. 6. Instantaneous snapshots of the suspension for spherical cells at $H/d=3.1$ (top) and 6.3 (bottom). The computational box is also shown.

cell become convex and concave, respectively, and the sharp cusps develop at the trailing edges. The computed shape is in qualitative agreement with the observed erythrocyte shapes in narrow capillaries at high velocities [9,54]. The maximum deformation occurs in the $x$-$y$ plane, and the cell shape remains nearly circular in the $x$-$z$ plane. The amount of deformation decreases and the sharp cusps disappear with decreasing Ca. 3D shapes of the biconcave cells in the single-file motion are shown in Fig. 5(b) at $t^*=0$ and $t^*=4.7$, respectively, for Ca=0.6. The cell shape in the $x$-$z$ plane remains biconcave, but that in the $x$-$y$ plane assumes the parachute shape. The dimple in the front of the cell is absent, but that in the rear becomes more prominent. Formation of the cusps at the trailing edges in the $x$-$y$ plane is observed. At Ca=0.05, the dimples are absent in the rear and front of the cell, and the overall shape resembles a cylindrical pellet (not shown).

We now consider the motion of multiple cells which is the main focus of this paper. The number of cells simulated varies from 2 to 122, the size ratio $H/d$ varies from 1.25 to 6.3, and the hematocrit $H_t$ varies from 5% to 26% (see Table I). At $t^*=0$, the cells are distributed randomly in the computation domain. Only for two runs, $H_t=5\%$ for $H/d=6.3$ and 4.5, a center-weighted distribution is taken to reduce the computation time since the lateral drift would eventually result into a higher cell concentration near the center. For all other runs, the cells span across the entire channel width. During the course of the simulations, the fluid and the cell velocity and the cell shape and coordinates are stored at frequent intervals which are postprocessed to obtain the time-averaged rheology.

Instantaneous cell shape and distribution from a few representative simulations are shown in Figs. 6 and 8. Figure 6(a) shows a snapshot of a three-file motion for $H/d=3.1$ for which the computational box contains 15 cells. A significant deformation in cell shapes is evident. The cells located near the channel walls form the slipper shapes. The computed shape is in qualitative agreement with the nonaxisymmetric single- or two-file motion of the erythrocytes at a high velocity in glass tubes with internal diameter of $\approx 10-15$ $\mu$m [9]. The cells flowing near the center deform less and have a convex surface at the front and a nearly flat surface at the rear. The cells near the center move with a higher velocity than those near the walls resulting in the binary collisions. Such collisions inhibit a continuous lateral drift of the cells flowing near the walls. The multifile motion is shown in Fig. 6(b) for $H/d=6.3$ with 122 cells in the computational box. The slipper shapes are no longer seen, rather, the cells near the walls are more ellipsoidal and disk shaped, and those near the center are nearly spherical. The binary collision affects the cell shapes significantly which is evident in the flattening of the cell surface and the appearance of the dimples.

Each simulation is run long enough so that the initial transience is passed. The mean quantities are extracted by averaging over a large time window over which the suspension remains statistically stationary. Figure 7 presents the time history of the relative apparent viscosity $\mu_{\mathrm{rel}}(t^*)$ for several runs which shows that the simulations were continued well beyond the initial relaxation time of the suspension. On the average, the cells in the simulations travel by a distance of about 15–50 computational boxes or 50–500 cell diameters. To test that the results are independent of the domain size, we repeat a case in Fig. 7 ($H/d=4.5$, $H_t=18\%$, $N_c=30$, Ca $=0.05$) on a domain that is twice the size in length and width ($2H\times 2H\times H$). The corresponding resolution is increased from $120\times 121\times 120$ to $240\times 241\times 120$, and the number of

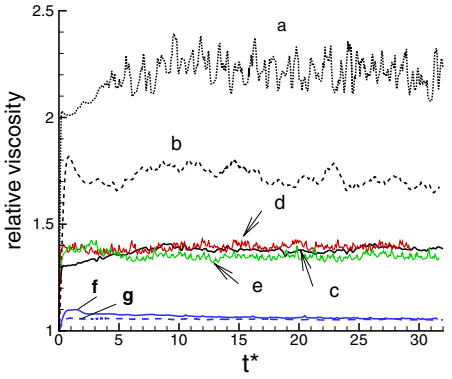


FIG. 7. (Color online) Time history of relative viscosity. (a) Dotted line: Ca=0.05, $H_t$=26%, and $H/d$=6.3; (b) dashed line: Ca=0.6, $H_t$=26%, and $H/d$=6.3; (c) solid black line: Ca=0.05, $H_t$=18%, and $H/d$=4.5; (d) solid red line: same as (c) but in larger domain $2H\times 2H\times H$; (e) solid green line: same as (c) but at higher resolution $240\times 241\times 240$, (f) solid blue line: $H_t$=5%, $H/d$=6.3, and Ca=0.6 with an initial random distribution of cells, and (g) dashed blue line: same as (f) but with a center-weighted initial distribution.

capsules is from 30 to 120. As shown in Fig. 7, the difference in the apparent viscosity in the two cases is insignificant. To test the adequacy of the flow resolution for capsule suspension, we repeat one case ($H/d$=4.5, $H_t$=18%, $N_c$=30, Ca =0.05) which was previously simulated using $120\times 121\times 120$ by doubling the resolution on each side. Only a small drop (<3%) in the relative viscosity is observed as shown in Fig. 7.

We further show in Fig. 7 two cases at $H_t$=5%, $H/d$ =6.3: one with a center-weighted initial distribution and another with cells randomly distributed across the channel. After the initial transience, both runs yield nearly the same apparent viscosity.

Visualizations from the multifile motion of the biconcave cells are shown in Fig. 8. As the flow develops, the cells near the walls rotate in accordance with the direction of the vorticity. However, the continuous tumbling motion that is present for a biconcave cell in a dilute suspension is no longer observed. Interaction with the neighboring cells inhibits a continuous tumbling. In some cases, such an interaction may cause a reversal of the direction of rotation. Eventually the cells near the wall align with the flow direction and do not show any further rotation. The alignment decreases with increasing distance from the wall and the cells near the center flow with a nearly vertical alignment. The cells near the wall deform more, lose their biconcave shape, and assume a disklike shape. Those near the channel center deform less and assume the parachute shapes. As the size ratio $H/d$ increases from 3.1 to 4.9 in Fig. 8, the parachute shapes near the channel center become less evident. We verified that the high degree of ordering in Fig. 8 is not the effect of domain size. At higher volume fractions, the cells flow in a stacklike close-packed manner with reduced randomness in their distribution. Formation of the cell-free layer is evident in Figs. 6 and 8. For the case of the spherical cells, the cell-free layer is formed under the balance of the center-ward lateral drift and the dispersion due to the binary collisions. For the case

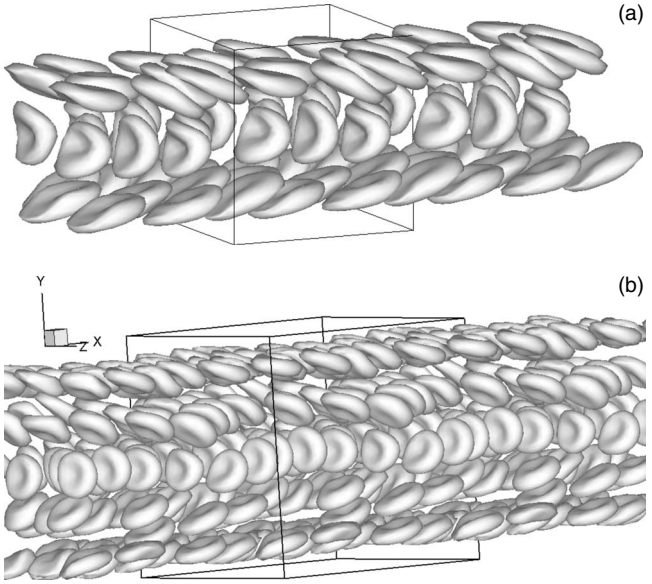


FIG. 8. Instantaneous snapshots of suspension of biconcave cells for $H/d$=3.1 (top) and $H/d$=4.9 (bottom). The computational box is also shown.

of the biconcave cells, the nearly horizontal alignment of the cells flowing near the walls apparently increases the width of the cell-free layer.

#### *1. Cell trajectory and velocity traces*

Figure 9 shows the lateral position ($y_c$) of the cell centroids which exhibit fluctuations due to the collisions with the neighboring cells. For Ca=0.6 and $H_t$=5% [Fig. 9(a)], the trajectories merge toward the center of the vessel with time indicating the axial streaming of the cells. However, unlike in a dilute suspension, a continuous lateral drift is not observed due to the interaction from the neighboring cells. When the cells with a reduced deformability are considered at Ca=0.005 [Fig. 9(b)], the lateral drift is no longer observed. The cells then flow in a stacklike layered manner and their trajectories are primarily determined by the cell-cell interactions. The formation of three layers of cells is clearly seen in Fig. 9(b) which is for Ca=0.005. Such a layered distribution is not prominent at a higher Ca. The lateral drift is inhibited when the hematocrit is increased from 5 to 18% as evident by comparing Figs. 9(a) and 9(c). The fluctuation in the lateral position increases at higher $H_t$ due to an increased cell-cell interaction.

Root mean square (rms) of the fluctuations in the lateral position ($y'$) and axial velocity ($u'$) can be used as a measure of the hydrodynamic dispersion in the suspension. Figure 10(a) shows the variation in $y'$ over the vessel cross section for two different values of $H_t$ and at fixed $H/d$=6.3 and Ca=0.05. Here the data are presented by averaging over bins of $\Delta y$=0.1. $y'$ increases toward the vessel center as the axial streaming of the cells results in an increase in the hematocrit and hence an increased cell-cell collision near the center. However, as $H_t$ increases, the variation in $y'$ becomes nearly uniform as the cell distribution becomes uniform. The range of $y'$ in Fig. 10(a) suggests that the lateral position of a cell

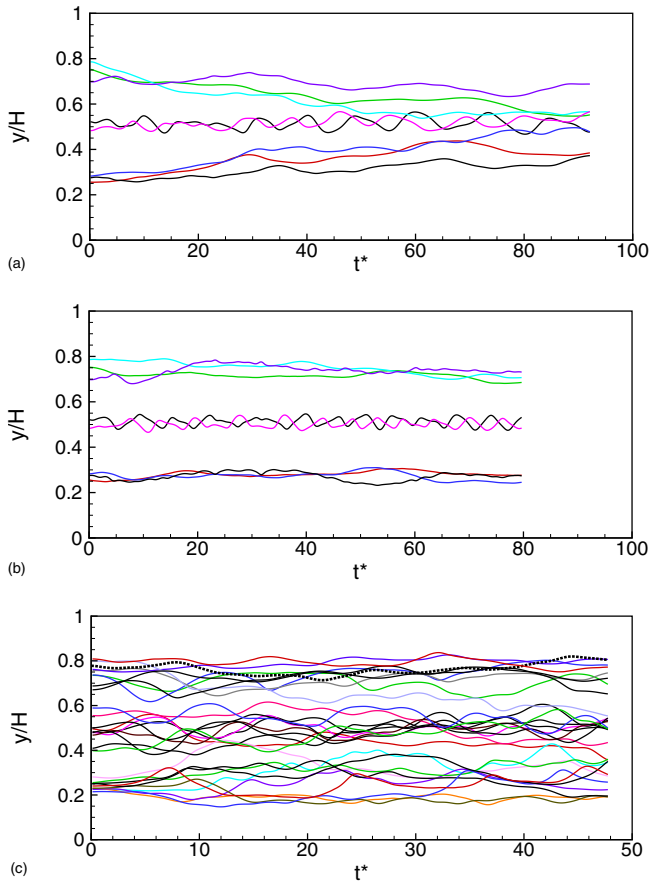


FIG. 9. (Color online) Sample cell trajectory for $H/d=4.5$. (a) Ca=0.6, $H_t=5\%$; (b) Ca=0.005, $H_t=5\%$; and (c) Ca=0.6, $H_t=18\%$.

fluctuates over 1%–25% of its diameter in our simulations. This is comparable to, but lower than, the *in vivo* data of Bishop *et al.* [36,37] which is also shown in Fig. 10(a). The effect of the cell deformability is considered in Fig. 10(b). The figure shows that the rms fluctuation increases with decreasing Ca and hence decreasing cell deformability. This is consistent with the previously published results on the binary collision of deformable particles which suggest that such interactions result in a higher lateral displacement for the nearly rigid cells than that for the deformable cells [55]. The effect of $H/d$ is considered in Fig. 10(c) which shows that the $y'$ profiles become more uniform with increasing $H/d$ due to the increased number of cells and hence increased number of collisions. The rms velocity fluctuation $u'$ is shown in Fig. 10(d). The velocity fluctuation decreases from the wall toward the center since it is scaled by the mean velocity $\overline{u_c}$ of each cell. The unscaled velocity fluctuation shows a similar trend as that of the position fluctuation $y'$. The dependence of $u'$ on $H_t$ is considered in the figure. The velocity fluctuation increases with increasing $H_t$ as $\overline{u_c}$ decreases (shown later in Fig. 13). The velocity fluctuations in the simulations vary from 1% to 10% of the mean velocity; in contrast, the *in vivo* data of Bishop *et al.* [36,37] give higher velocity fluctuations as it did for the rms position $y'$.

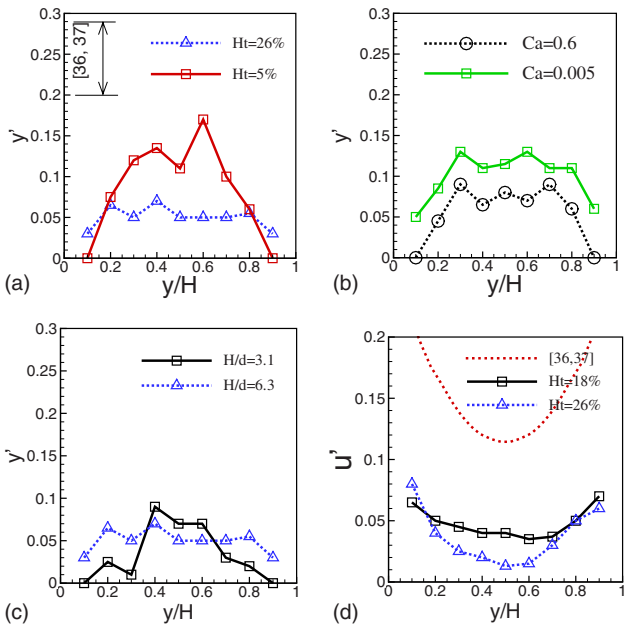


FIG. 10. (Color online) [(a)–(c)] rms fluctuation $y'$ over channel cross section showing the effect of hematocrit, Ca, and $H/d$, respectively. (d) rms velocity fluctuation showing the effect of hematocrit at $H/d=6.3$ and Ca=0.05. Also shown is the *in vivo* data of Bishop *et al.* [36,37].

### 2. Cell-free layer

The simulations allow us a direct estimation of the cell-free layer thickness. This is done by extracting the cross-sectional variation in local hematocrit $H_c(y)$. As mentioned before, due to lateral drift of the cells, local hematocrit is higher near the center and lower near the wall. The indicator function $I(x,y,z,t)$, as described in Eq. (9), can be used to calculate $H_c(y,t)$ which is then time averaged to obtain $H_c(y)$. Figure 11 shows the ratio $H_c(y)/H_t$ for some representative cases. The ratio goes to zero near the wall indicating the depletion of the cells, and it is around one near the center. The oscillating nature of $H_c(y)/H_t$ near the center of the vessel is due to the cells flowing in layers as described earlier in Fig. 9. The width of the cell-free layer, denoted by $\delta$, can be precisely calculated from such plots and is given in Fig. 12 in a dimensionless form as $\delta/(H/2)$. We see from

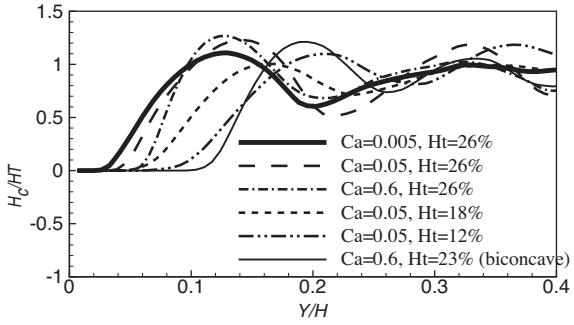


FIG. 11. Cross-sectional variation in hematocrit. Results are shown for half channel width; $y/H=0$ is the wall and $y/H=0.5$ is the center of the channel.

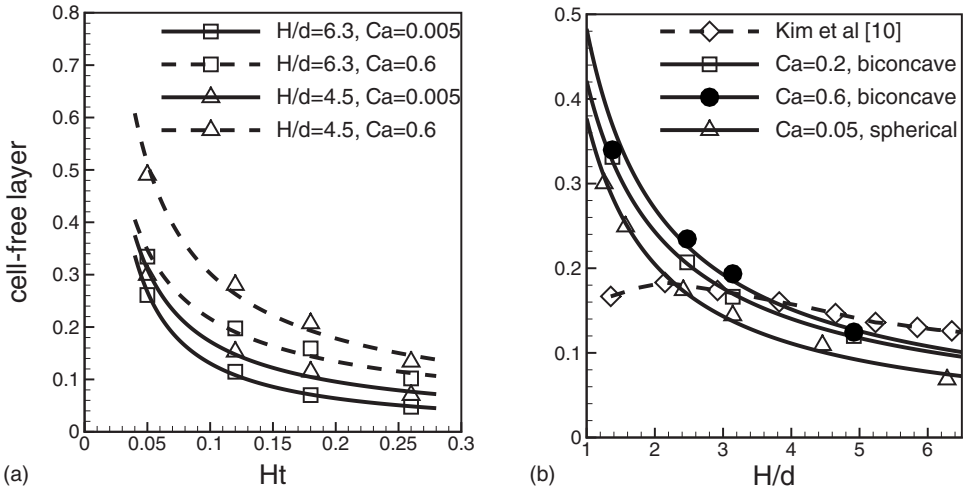


FIG. 12. Dimensionless cell-free layer width $\delta/(H/2)$ as a function of (a) $H_t$ for two values of Ca and $H/d$ for spherical cells and (b) as a function of $H/d$ for biconcave and spherical cells for $H_t=26\%$. Also shown in (b) is the *in vivo* data of Kim *et al.* [10].

Fig. 12(a) that $\delta/(H/2)$ decreases with the increasing hematocrit and decreasing Ca. The reduction is due to a reduced lateral drift of the cells with the increasing hematocrit and decreasing Ca as shown earlier in Fig. 9. Figure 12(b) shows that $\delta/(H/2)$ decreases with an increasing vessel size. Also presented in this figure is the *in vivo* data from [10]. The simulations predict a lower value of $\delta/(H/2)$ in comparison to the *in vivo* data, though a qualitative agreement is observed between the two.

Also note in Fig. 11 that $H_c(y)$ approaches its value at the core smoothly rather than a sudden step change assumed in the two-phase models for the blood flow in small vessels (to be discussed later). The rate of increase in $H_c(y)$ across the interface of the cell-free layer and the core region decreases with increasing Ca and decreasing $H_t$. This is because the highly elongated cells at a higher Ca favors a more close-packed distribution and hence a higher slope of $H_c(y)$. In contrast, a lower hematocrit causes an increased cell-to-cell separation distance and hence a reduced slope of $H_c(y)$. As will be shown later, these results have consequences in the modeling of the blood flow in microvessels.

### 3. Plug-flow profile

The mean blood velocity over the vessel cross section, compared with the Poiseuille velocity, is shown in Fig. 13. The mean velocity decreases with increasing $H/d$ [Fig. 13(a)]. This is because the increasing $H/d$ results in the increasing number of cells, and hence more interfacial contacts, causing an increased energy dissipation and hence a reduced blood flow. For $H/d=6.3$, the maximum velocity is reduced to about 35% of the centerline velocity of the Poiseuille flow. Experimental measurements using blood have shown the well-known plug-flow profile which is characterized by a parabolic velocity near the wall and a nearly constant velocity near the vessel center. The simulation results show a prominent plug-flow profile for the smallest vessel considered here ($H/d=1.25$) in which the single-file motion occurs. As $H/d$ increases, the computational velocity profile departs from the plug-flow toward a blunt parabola. A qualitative comparison of this trend can be made with the *in vivo* measurements of Bishop *et al.* [36,37] who obtained an empirical relation $u/U_{\max}=1-(r/R)^k$ with $k$ in the range of 2.1–2.2 for the blood flow in 45–75 $\mu$m venules. A plug-flow profile occurs when $k\approx 3$, and a parabolic profile occurs when $k=2$. The present numerical results also predict values of $k$ in the same range as that of Bishop *et al.* [36,37].

The mean velocity decreases with the increasing hematocrit [Fig. 13(b)]. At $H_t=26\%$, the maximum centerline velocity reduces to about 30% of the parabolic flow. The reduction in the mean velocity is also due to the increased energy dissipation that results from an increasing $H_t$. The mean velocity also decreases with decreasing Ca [Fig. 13(c)].

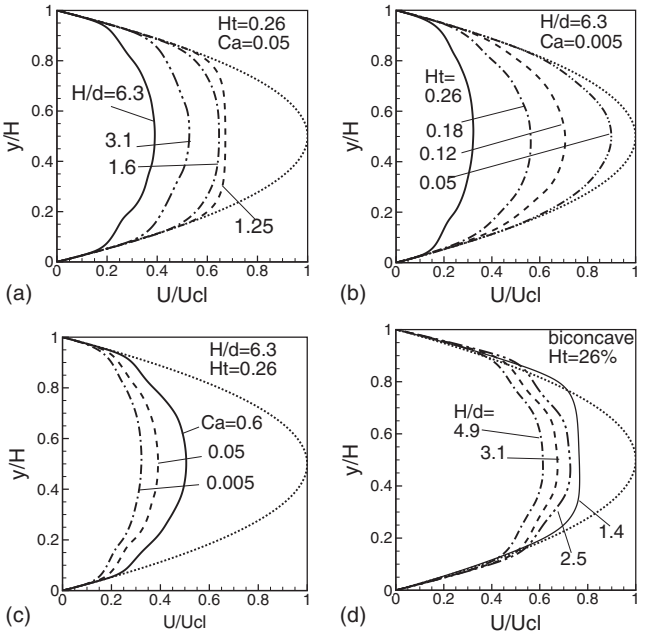


FIG. 13. Mean velocity profile. Dotted line is the parabolic flow. Effect of (a) $H/d$, (b) hematocrit, and (c) cell deformability for spherical cell suspension. (d) Effect of $H/d$ for biconcave cell suspension.

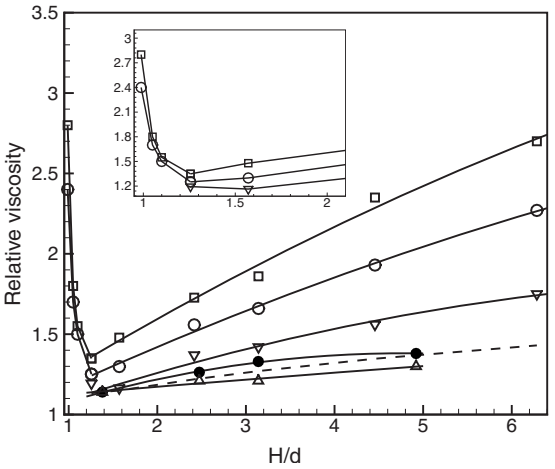


FIG. 14. Variation in relative apparent viscosity $\mu_{rel}$ as a function of vessel size for different Ca at $H_t$=26%. Symbols represent the computed values, and the solid lines are the second-order fit through the data. Results for spherical cells are shown for Ca =0.005 (—□—), Ca=0.05 (—○—), and Ca=0.6 (—▽—). Results for biconcave capsules are shown for Ca=0.05 (—●—) and Ca =0.2 (—△—). The dashed line is the correlation of Pries *et al.* [3]. The inset shows the results for lower range of $H/d$.

This is likely due to an additional energy loss caused by the increased fluctuation in the cell velocity as shown earlier in Figs. 9 and 10. The relative decrease in the mean velocity is however more sensitive to $H_t$ and $H/d$ than Ca. The maximum centerline velocity drops by a factor of 3 as $H_t$ is increased by a factor of 5.2 [Fig. 13(b)], whereas it drops by a factor of 1.7 as Ca is reduced by a factor of 120.

The mean velocity for the biconcave cells is shown in Fig. 13(d) for the varying vessel size. As in the case of the spherical cells, the mean velocity decreases with the increasing $H/d$. The variation with respect to Ca and $H_t$ is also qualitatively similar for the biconcave and spherical cells, and hence not repeated.

#### *4. Fahraeus-Lindqvist effect*

The computed relative apparent viscosity $\mu_{rel}$ is shown in Fig. 14 as a function of $H/d$ for three values of Ca. As evident in the figure, the computed $\mu_{rel}$ decreases with a decreasing $H/d$. Thus, the Fahraeus-Lindqvist effect is qualitatively predicted by our simulations. The computational results are compared with an empirical relation developed by Pries *et al.* [3] based on the blood flow *in vitro*. The simulation results for the biconcave cells agree well with the empirical relation. The effect of the cell deformability on the relative viscosity can also be inferred from Fig. 14. $\mu_{rel}$ is observed to increase with a decreasing Ca. This is likely due to two reasons. First, the increased fluctuation (Figs. 9 and 10) in the cell velocity at a reduced Ca causes an increased energy dissipation and hence a higher apparent viscosity. Second, a decreasing width of the cell-free layer at a reduced Ca, as shown in Fig. 12, also leads to a higher apparent viscosity. Further, the effect of Ca is significant in the larger vessels. An increase in $\mu_{rel}$ with an increasing $H/d$ is more rapid at a lower Ca than at a higher Ca.

Figure 14 also shows that $\mu_{rel}$ for the biconcave cells is less than that for the spherical cells when other parameters are kept constants. This may appear surprising since for the same $H_t$ and $H/d$, the suspension contains nearly twice the number of biconcave cells than that of the spherical cells (Table I). Hence the interfacial energy loss is expected to be higher for the biconcave cells. This additional energy loss, however, is compensated by a larger width of the cell-free layer for the biconcave cells as seen earlier in Figs. 11 and 12. As mentioned earlier in the context of Fig. 8, the larger width of the cell-free layer arises due to the near horizontal alignment of the biconcave cells flowing near the wall.

Experiments using the erythrocyte suspension in capillary glass tubes showed that decreasing the tube diameter below $\approx 10$ $\mu$m results in a *reverse* Fahraeus-Lindqvist effect, that is, the relative viscosity increases with the decreasing tube diameter [3]. This is due to the transition from the multifile to the single-file mode in which the cells flow in a tightly fit manner. The relative viscosity attains its lowest values for tube diameter $\approx 10$ $\mu$m for the normal erythrocytes. The simulation results for the lower range of $H/d$ for Ca=0.005 and 0.05 clearly show a reversing trend of $\mu_{rel}$ for $H/d < 1.25$. We also compute $H_t/H_d = \bar{U}/\overline{U_c}$ which is the ratio of the mean (time- and space-averaged) blood velocity to the mean (time- and ensemble-averaged) cell velocity. Our simulations qualitatively predicted the Fahraeus effect that $H_t/H_d$ increases with increasing $H/d$ approaching unity. A reversing trend is also observed with tightly fit single-file motion at lower $H/d$. We also observe that unlike in $\mu_{rel}$, the dependence of $H_t/H_d$ on Ca is relatively weak. However, the simulations predicted higher values than those of Pries *et al.* [3]. Perhaps, the difference can be due to geometrical effect (circular tube vs parallel plates) or the limitation of the immersed boundary method that the cells do not come too close to each other in the computation.

### C. Comparison of simulation results with two-phase model

Flow of blood in microvessels is often described by a two-phase model [9,13–15] in which the vessel is divided into a cell-free region of thickness $\delta$ and a core region of $H-2\delta$. Then

$$\mu(y) = \mu_f + (\mu_c - \mu_f)\mathcal{H}(y-\delta) \quad \text{for } 0 \le y \le H/2, \tag{13}$$

$$\mu(y) = \mu_c + (\mu_f - \mu_c)\mathcal{H}(y-H+\delta) \quad \text{for } H/2 \le y \le H, \tag{14}$$

where $\mu_f$ and $\mu_c$ are the viscosity of the cell-free and core regions, respectively, and $\mathcal{H}$ is the Heaviside function. The mean velocity is

$$u_f(y) = -\frac{dP}{dx}\frac{H^2}{2\mu_f}\left(\frac{y}{H} - \frac{y^2}{H^2}\right) \quad \text{for } 0 \le y \le \delta, \tag{15}$$

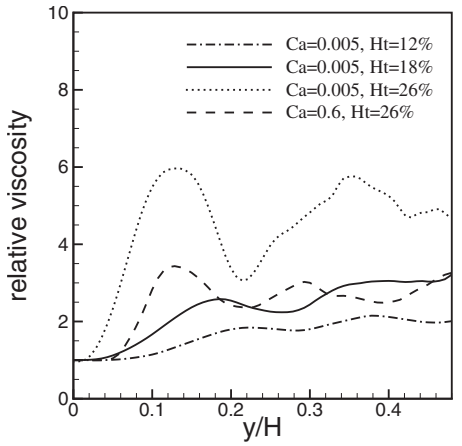


FIG. 15. Cross-sectional variation in apparent viscosity obtained *a posteriori* from the simulations for some sample cases for $H/d=6.3$. Results are shown for half channel width; $y/H=0$ is the wall and $y/H=0.5$ is the center.

$$u_c(y) = -\frac{dP}{dx}\frac{H^2}{2\mu_f}\left[\frac{\mu_f}{\mu_c}\left(\frac{y}{H}-\frac{y^2}{H^2}\right)+\left(1-\frac{\mu_f}{\mu_c}\right)\times\left(\frac{\delta}{H}-\frac{\delta^2}{H^2}\right)\right] \quad \text{for} \quad \delta \le y \le H/2, \tag{16}$$

where $u_f(y)$ and $u_c(y)$ are the velocity of the cell-free and core regions, respectively. The values of the three unknown parameters in the above model, $\delta$, $\mu_f$, and $\mu_c$, are often taken *ad hoc* to match the experimental data of the relative apparent viscosity. While the recent high-resolution measurements [4,10] have yielded the values of $\delta$, the experimental data on $\mu_f$ and $\mu_c$ are scarce.

In reality, the interface between the core and the cell-free layers cannot be well defined as assumed in the two-phase model. The cells are continuously dispersed across the interface due to the hydrodynamic interaction as observed in our simulations and elsewhere [10]. Thus the variation in the apparent viscosity across the vessel is expected to be smooth rather than a step jump as assumed in the two-phase model [Eqs. (12) and (13)]. Based on the micro-particle image velocimetry (PIV) measurements of blood velocity, Long *et al.* [7] and Damiano *et al.* [4] showed that $\mu(y)$ varies smoothly across the vessel and it approaches $\mu_f$ near the wall and $\mu_c$ near the center.

The cross-sectional variation in $\mu(y)$ can be extracted from the present numerical data by using the relation

$$\frac{\mu(y)}{\mu_p} = \frac{\dot{\gamma}_p(y)}{\dot{\gamma}(y)}, \tag{17}$$

where $\dot{\gamma}$ and $\dot{\gamma}_p$ are the shear rates for the suspension and the Poiseuille flow, respectively. The computed values of $\mu(y)/\mu_p$ are shown in Fig. 15. As expected, $\mu(y)/\mu_p$ approaches unity near the wall, and it is higher in the core region of the vessel. In the core region, it is often nonmonotonic with respect to $y$. The local maximum and minimum of $\mu(y)/\mu_p$ corresponds to the local maximum and minimum of $H_c(y)$ shown earlier in Fig. 11 implying a high viscous dissipation near the regions of interfacial contacts. The most important feature of Fig. 15 is that $\mu(y)/\mu_p$ varies smoothly across the interface of the core and the cell-free layer, unlike the step jump assumed in the two-phase model. Such a smooth variation in $\mu(y)/\mu_p$ as obtained in the simulations is in qualitative agreement with the earlier micro-PIV measurement [4,7]. The figure also shows that the slope of $\mu(y)/\mu_p$ across the interface of the cell-free and the core regions is highly dependent on $H_t$, and it increases with increasing $H_t$.

We can now calculate $\mu_f$ and $\mu_c$ as

$$\mu_f = \frac{1}{\delta}\int_0^{\delta}\mu(y)dy, \quad \mu_c = \frac{1}{H/2-\delta}\int_{\delta}^{H/2}\mu(y)dy, \tag{18}$$

which are listed in Table II. First we note that the cell-free layer viscosity $\mu_f$ is slightly higher than the plasma viscosity $\mu_p$. This is likely due to the occasional intrusion of the cells from the core region into the cell-free layer caused by the hydrodynamic dispersion. The difference between $\mu_f$ and $\mu_p$ increases with the increasing hematocrit and decreasing Ca. Second, the core viscosity $\mu_c$ is significantly higher than the cell-free layer viscosity and also higher than the effective viscosity of the whole suspension shown earlier in Fig. 14. The core viscosity $\mu_c$ increases with increasing hematocrit and decreasing Ca due to the increased interfacial dissipation.

TABLE II. Viscosity of the core ($\mu_c$) and cell-free layer ($\mu_f$) and the thickness $\beta$ of the transition layer obtained from the simulations.

| $H/d$ | Ca | $H_t$ | $\mu_f/\mu_p$ | $\mu_c/\mu_p$ for two-phase model | $\mu_c/\mu_p$ for three-layer model | $\beta/(H/2)$ | $(\beta-\delta)/(H/2)$ |
|---|---|---|---|---|---|---|---|
| 6.3 | 0.005 | 26 | 1.05 | 5.11 | 5.52 | 0.21 | 0.16 |
| | 0.05 | 26 | 1.05 | 4.02 | 4.25 | 0.20 | 0.13 |
| | 0.6 | 26 | 1.02 | 2.93 | 3.06 | 0.22 | 0.12 |
| | 0.005 | 18 | 1.02 | 2.45 | 2.68 | 0.37 | 0.30 |
| | 0.05 | 18 | 1.02 | 2.23 | 2.46 | 0.31 | 0.22 |
| | 0.6 | 18 | 1.00 | 2.01 | 2.06 | 0.35 | 0.19 |
| | 0.05 | 12 | 1.00 | 1.75 | 1.91 | 0.41 | 0.27 |
| 4.5 | 0.005 | 26 | 1.09 | 4.98 | 5.03 | 0.20 | 0.13 |
| | 0.05 | 26 | 1.04 | 3.82 | 3.90 | 0.22 | 0.12 |

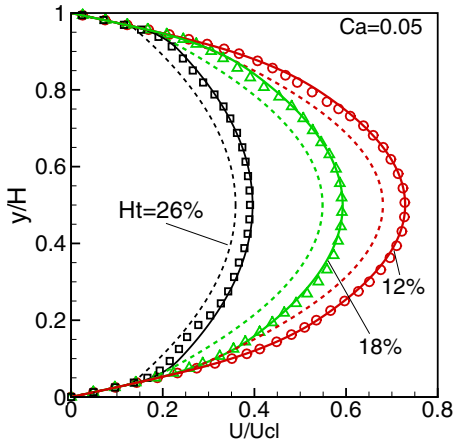


FIG. 16. (Color online) Comparison of mean velocity obtained from simulations (symbols) and predicted by two-phase model [Eqs. (14) and (15)], dotted lines, and three-layer model [Eqs. (22)–(24)], continuous lines. Results are shown for $H/d=6.3$ and Ca=0.05 and for different $H_t$. Similar comparison is observed for other runs.

Using the values of $\mu_c$ and $\mu_f$ given in Table II, the velocity profile from the two-phase model [Eqs. (14) and (15)] is obtained and compared with the velocity profile obtained directly from the simulations (Fig. 16). We see that the two-phase model underpredicts the mean velocity. The difference between the simulations results and the two-phase model prediction could be as high as 40% depending on the $y$ location.

### D. Three-layer model of blood flow in microvessels

The above result suggests that a model that takes into consideration the $y$ dependence of viscosity in the vicinity of $y=\delta$ would give a better agreement with the simulation result. In this model the vessel is divided in three layers: a cell-free layer of thickness $\delta$ of a constant viscosity $\mu_f$, a transition layer of thickness $\beta-\delta$ wherein the viscosity varies *linearly* with $y$, and a core region of half-width $H/2-\beta$ of a constant viscosity $\mu_c$. Thus,

$$\text{cell-free layer: } \mu(y)=\mu_f \quad \text{for } 0\le y\le \delta, \tag{19}$$

$$\text{transition layer: } \mu(y)=\mu_f+\frac{\mu_c-\mu_f}{\beta-\delta}(y-\delta) \quad \text{for } \delta\le y\le \beta, \tag{20}$$

$$\text{core: } \mu(y)=\mu_c \quad \text{for } \beta\le y\le H/2. \tag{21}$$

Note that in this model $\mu_c$ must be calculated as

$$\mu_c=\frac{\int_0^H \mu(y)dy-\mu_f(\beta+\delta)}{H-(\beta+\delta)}, \tag{22}$$

where $\mu(y)$ is obtained from the simulation results as given in Fig. 15. The linear variation in the viscosity in the transition layer as assumed here can be improved further. However, as will be shown later, even such a linear variation can lead to a better agreement with the simulation results.

The mean velocities are

$$u_f=-\frac{dP}{dx}\frac{1}{2\mu_f}(yH-y^2), \tag{23}$$

$$u_\beta=-\frac{dP}{dx}\left(\frac{\beta-\delta}{\mu_c-\mu_f}\right)\left[-y+\left(\frac{\beta\mu_f-\delta\mu_c}{\mu_c-\mu_f}+\frac{H}{2}\right)\ln\left(\frac{\mu_c}{\mu_f}\right)+\left(\frac{\mu_c}{\mu_f}-1\right)\frac{H\delta-\delta^2}{2(\beta-\delta)}+\delta\right], \tag{24}$$

$$u_c=-\frac{dP}{dx}\frac{1}{2\mu_c}\left[yH-y^2-\frac{2(\beta-\delta)^2}{1-\mu_f/\mu_c}\times\left(1+\frac{\beta\mu_f-\delta\mu_c+(\mu_c-\mu_f)H/2}{\beta-\delta}\ln\frac{\mu_f}{\mu_c}\right)+(H\delta-\delta^2)\frac{\mu_c}{\mu_f}+\beta^2-H\beta\right], \tag{25}$$

where $u_f$, $u_\beta$, and $u_c$ are the velocities in the cell-free layer, transition layer, and core, respectively.

The values of the parameters $\beta$, $\beta-\delta$, and $\mu_c$, obtained from *a posteriori* analysis of the simulation data, are given in Table II. We see that $\beta$ does not show any strong dependence on Ca or $H$, but it increases with decreasing $H_t$. The thickness of the transition layer $\beta-\delta$, however, depends on hematocrit and Ca. It decreases with increasing Ca. This is because the elongated cell shapes at a higher Ca allow a more close-packed arrangement in the vicinity of $y=\delta$. It also decreases with increasing $H_t$ due to the reduced cell-cell separation distance. Most importantly, as seen from Table II, the width of the transition layer is comparable to that of the cell-free layer. Thus, the transition layer is expected to play a major role in determining the blood velocity profile. Also note in Table II that the core viscosity $\mu_c$ for the three-layer model is higher than that for the two-phase model due to the introduction of the transition layer.

The prediction based on the three-layer model gives an excellent agreement with the simulation results as shown in Fig. 16.

## V. SUMMARY AND CONCLUSION

Three-dimensional computational modeling and simulation of multiple deformable cells flowing in microvessels, typical of microcirculation and microfluidic devices, are presented. The major contribution of this paper is the computational framework that can resolve the dynamics of individual deformable cell with high fidelity, yet can consider a large number of hydrodynamically interacting cells, up to O(100) in number, in a semidense suspension, as in case of the flowing blood. We focus on how the collective dynamics of many cells leads to the physiologically relevant processes such as development of the cell-free layer and the Fahraeus-Lindqvist effect under varying cell deformability as in case of normal and pathological blood.

Flow visualization and analysis of cell trajectory and velocity of the multifile motion are presented. The results presented here include, e.g., the variation in the local hematocrit over the vessel cross section obtained *a posteriori* from the simulation data, which in turn yields the width of the cell-free layer $\delta$. A statistically stationary cell-free layer is developed under a balance of the lateral drift and the hydrodynamic dispersion resulting from the cell-cell collision. Our results show that $\delta/(H/2)$ decreases with increasing vessel size, increasing hematocrit, and decreasing Ca. Simulation results also predicted the well-known plug-flow profile and the Fahraeus-Lindqvist effect. The role of the cell deformability on these physiologically important processes is presented. We also present the variation in the *local* apparent viscosity across the vessel and show that it increases rather slowly over the interface of the cell-free and core layers. We further illustrate how the local viscosity varies as the cell deformability is altered as in case of many hemodynamic disorders.

Comparisons with previous experimental data presented here are meant to be qualitative as the simulations represent flow in microchannels while the experiments are performed either in glass tubes of circular cross section or *in vivo*. It is, however, interesting to note the qualitatively similar trend (e.g., in $\mu_{\mathrm{rel}}$, $u'$, etc.) in both geometries. One limitation of the simulations is that the immersed boundary method implemented here does not allow the cells to physically contact each other yielding a higher intercellular spacing in the simulated blood flow. This may result in a reduced rms fluctuation and a reduced width of the cell-free layer in our computations. It should also be emphasized that the area-incompressibility condition is imposed here only for the biconcave cells and not for the spherical cells. This difference must be considered while comparing the results for the two unstressed shapes as presented in Figs. 5 and 14 and others.

We further show that the two-phase model of blood flow in microvessels underpredicts the mean velocity obtained in the simulations by as much as 40%. This also implies that the two-phase model would underpredict the flow rate and hence overpredict the relative apparent viscosity. It must be emphasized that despite the difference between the two-phase model and the simulation results, the former has been shown to agree with *in vitro* blood velocity. This agreement, however, depends on the *ad hoc* choice of the empirical constants $\delta$, $\mu_f$, and $\mu_c$. It is then argued that the difference between the model and the simulation results is due to the steplike jump of the viscosity and local hematocrit at the interface of the cell-free layer and the core layer assumed in the model. In contrast, the simulations show that the local viscosity and hematocrit increase smoothly across the interface. This observation is consistent with a recent $\mu$PIV measurement of blood flow *in vivo* [4,7]. The two-phase flow model overestimates the viscosity in the region immediately outside the cell-free layer compared to that obtained in the simulation. This overestimation results in an underprediction of the mean blood velocity. The simulation results, however, match very well with the core-annular-type models when we introduce a *transition* layer located between the cell-free layer and the core region in which the viscosity is assumed to increase linearly. A close-form expression of the velocity profile for this three-layer model is presented. The width of the transition layer is extracted from the simulation data and is shown to be comparable to the width of the cell-free layer. Thus the transition layer is expected to play a major role in determining the mean blood velocity and hence the relative viscosity. By introducing the transition layer, the model adds more physics, as the extent of this layer is directly correlated with the energy dissipation rate across the core-plasma-layer interface that is a function of the cell deformability and hematocrit.

The results presented here signify the predictive capability of such detailed computations. To the best of our knowledge, this paper is one of the very few recently published works where 3D modeling of multiple deformable cells is considered. High fidelity computational modeling of the flow of multiple deformable interacting cells, without sacrificing detailed dynamics of individual cell, is a nontrivial and challenging task, and this is where the contribution of the present paper stands. Excellent contributions are being made even in recent days on dynamics of a single cell or capsule in flow. Very few works exist that attempt to consider interaction of multiple cells in dense suspension without sacrificing the detailed dynamics of individual cell. In our present work, we take the modeling capability to a level where hemorheological phenomena can be predicted by detailed particle-scale models. If the microrheology is of interest, as in the present paper, perhaps there is no other "alternative" approach but to consider such detailed particle-scale simulations. Perhaps also, this is another work where quantities of physiological importance (and of importance to suspension flow), e.g., particle-free region and Fahraeus-Lindqvist effect, as a function of cell deformability, are obtained directly from such rare particle-scale simulations. The low-order model presented here can be of significance to researchers in physiological flows, suspension flows, and in general complex flows. This also shows the predictive ability of the detailed particle-scale simulations considered here. The simulations have generated a database with a wealth of information on the dynamics of flowing cell suspension which can be further postprocessed to gain deeper insight in the general problem of suspension of deformable particles and of erythrocytes, in particular. For example, the simulation results can be used to obtain collision frequency of cells as a function of cell deformability, hematocrit, and vessel size, which is of importance in modeling erythrocyte aggregation. The coefficients of hydrodynamic dispersion of cells and that of tracer particles can also be obtained, which are of importance in solute and drug transport in microvessels.

## ACKNOWLEDGMENTS

This research was funded by NSF under Grants No. BES-0603035 and No. CTS-0625936. Computational support from the SDSC and NERSC is acknowledged.

[1] A. S. Popel and P. C. Johnson, Annu. Rev. Fluid Mech. **37**, 43 (2005).
[2] H. L. Goldsmith, G. R. Cokelet, and P. Gaehtgens, Am. J. Physiol. **257**, H1005 (1989).
[3] A. R. Pries, D. Neuhaus, and P. Gaehtgens, Am. J. Physiol. Heart Circ. Physiol. **263**, H1770 (1992).
[4] E. R. Damiano, D. S. Long, and M. L. Smith, J. Fluid Mech. **512**, 1 (2004).
[5] R. Fahraeus and T. Lindqvist, Am. J. Physiol. **96**, 562 (1931).
[6] G. R. Cokelet and H. L. Goldsmith, Circ. Res. **68**, 1 (1991).
[7] D. S. Long, M. L. Smith, A. R. Pries, K. Ley, and E. R. Damiano, Proc. Natl. Acad. Sci. U.S.A. **101**, 10060 (2004).
[8] T. W. Secomb, B. Styp-Rekowska, and A. R. Pries, Ann. Biomed. Eng. **35**, 755 (2007).
[9] T. W. Secomb, in *Modeling and Simulation of Capsules and Biological Cells*, edited by C. Pozrikidis (Chapman and Hall, London, 2003).
[10] S. Kim, R. L. Kong, A. S. Popel, M. Intaglietta, and P. C. Johnson, Am. J. Physiol. Heart Circ. Physiol. **293**, H1526 (2007).
[11] J. Happel and H. Brenner, *Low Reynolds Number Hydrodynamics* (Kluwer, Dordrecht, 1983).
[12] H. L. Goldsmith, Fed. Proc. **30**, 1578 (1971).
[13] M. Sharan and A. S. Popel, Biorheology **38**, 415 (2001).
[14] T. W. Secomb, in *Biological Fluid Mechanics*, edited by C. P. Ellington and T. J. Pedley (Cambridge University Press, Cambridge, 1995).
[15] T. W. Secomb, Microvasc. Res. **34**, 46 (1987).
[16] S. R. Keller and R. Skalak, J. Fluid Mech. **120**, 27 (1982).
[17] S. Ramanujan and C. Pozrikidis, J. Fluid Mech. **361**, 117 (1998).
[18] C. D. Eggleton and A. S. Popel, Phys. Fluids **10**, 1834 (1998).
[19] C. Pozrikidis, Ann. Biomed. Eng. **31**, 1194 (2003).
[20] E. Lac, A. Morel, and D. Barthes-Biesel, J. Fluid Mech. **573**, 149 (2007).
[21] J. M. Skotheim and T. W. Secomb, Phys. Rev. Lett. **98**, 078301 (2007).
[22] T. W. Secomb, R. Skalak, N. Ozkaya, and J. F. Gross, J. Fluid Mech. **163**, 405 (1986).
[23] R. Hsu and T. W. Secomb, J. Biomech. Eng. **111**, 147 (1989).
[24] C. Coulliette and C. Pozrikidis, J. Fluid Mech. **358**, 1 (1998).
[25] A. Leyrat-Maurin and D. Barthes-Biesel, J. Fluid Mech. **279**, 135 (1994).
[26] C. Pozrikidis, Ann. Biomed. Eng. **33**, 165 (2005).
[27] P. R. Zarda, S. Chien, and R. Skalak, in *Computational Methods for Fluid-Solid Interaction Problems*, edited by T. Belytschko and T. L. Geers (American Society of Mechanical Engineers, New York, 1977).
[28] C. Sun and L. L. Munn, Biophys. J. **88**, 1635 (2005).
[29] J. Zhang, P. C. Johnson, and A. S. Popel, Phys. Biol. **4**, 285 (2007).
[30] P. Bagchi, Biophys. J. **92**, 1858 (2007).
[31] E. Jiang Ding and C. K. Aidun, Phys. Rev. Lett. **96**, 204502 (2006).
[32] M. M. Dupin, I. Halliday, C. M. Care, L. Alboul, and L. L. Munn, Phys. Rev. E **75**, 066707 (2007).
[33] I. V. Pivkin, P. D. Richardson, and G. Karniadakis, Proc. Natl. Acad. Sci. U.S.A. **103**, 17164 (2006).
[34] J. B. Freund, Phys. Fluids **19**, 023301 (2007).
[35] H. Zhao, J. B. Freund, and R. D. Moser, J. Comput. Phys. **227**, 3114 (2008).
[36] J. J. Bishop, P. Nance, A. S. Popel, M. Intaglietta, and P. C. Johnson, Am. J. Physiol. **280**, H222 (2001).
[37] J. J. Bishop, A. S. Popel, M. Intaglietta, and P. C. Johnson, Am. J. Physiol. **283**, H1985 (2002).
[38] Y. C. Fung and S. S. Sobin, J. Appl. Physiol. **26**, 472 (1969).
[39] R. Skalak, A. Tozeren, P. R. Zarda, and S. Chien, Biophys. J. **13**, 245 (1973).
[40] E. A. Evans and R. Skalak, *Biomembranes* (CRC, Boca Raton, FL, 1980).
[41] D. Boal, *Mechanics of the Cell* (Cambridge University Press, New York, 2002).
[42] J. Li, M. Dao, C. T. Lim, and S. Suresh, Biophys. J. **88**, 3707 (2005).
[43] Y. C. Fung, *Biomechanics: Mechanical Properties of Living Tissues* (Springer, Berlin, 1993).
[44] G. Tryggvason, B. Bunner, A. Esmaeeli, N. Al-Rawahi, W. Tauber, J. Han, S. Nas, and Y. Jan, J. Comput. Phys. **169**, 708 (2001).
[45] C. S. Peskin, J. Comput. Phys. **25**, 220 (1977).
[46] L. A. Miller and C. S. Peskin, J. Exp. Biol. **208**, 195 (2005).
[47] J. M. Charrier, S. Shrivastava, and R. Wu, J. Strain Anal. Eng. Des. **24**, 55 (1989).
[48] S. Shrivastava and J. Tang, J. Strain Anal. Eng. Des. **28**, 31 (1993).
[49] S. K. Doddi and P. Bagchi, Int. J. Multiphase Flow **34**, 966 (2008).
[50] H. Rehage, M. Husmann, and A. Walter, Rheol. Acta **41**, 292 (2002).
[51] D. Barthes-Biesel and J. M. Rallison, J. Fluid Mech. **113**, 251 (1981).
[52] M. Abkarian, M. Faivre, and A. Viallat, Phys. Rev. Lett. **98**, 188302 (2007).
[53] G. B. Jeffery, Proc. R. Soc. London, Ser. A **102**, 161 (1922).
[54] F. Risso, F. Colle-Paillot, and M. Zagzoule, J. Fluid Mech. **547**, 149 (2006).
[55] M. Loewenberg and E. J. Hinch, J. Fluid Mech. **338**, 299 (1997).